NUMERICAL SIMULATION OF THE TURBULENT FLOW PAST UPWIND YACHT SAILS

S. J. COLLIE, M. G. GERRITSEN, AND M. J. O'SULLIVAN

Abstract. The flow past upwind yacht sails is simulated using the commercial computational fluids dynamics software FLUENT. The high Reynolds number of the flows dictates the use of turbulence models. The two–equation models available in FLUENT at the time of this work ($k-\epsilon$, RNG $k-\epsilon$ and realizable $k-\epsilon$) are tested thoroughly using the backward facing step problem prior to their application to sail flows. The backward facing step problem is suitable as the flow involves complex turbulent behavior that is similar in nature to the flow past upwind sails. Two near–wall modelling options (wall functions and near–wall zonal model) are included in the tests. The realizable $k-\epsilon$ model with wall functions is shown to be the best available method in the package. Simulations of flow past two–dimensional sail sections confirm this result. Computations were also carried out for two different mast designs. Solutions of three–dimensional flows past America's Cup upwind sails were found to be useful for qualitative comparisons. Both 2D and 3D viscous flow results compare favorably to the results calculated by panel methods traditionally used in the sailing industry.

1. Introduction

As evident from the special issue on sail flow analysis of this journal [7] (1996), Computational Fluid Dynamics (CFD) is frequently used in the sail design process. Traditional computational packages in sail design are mostly based on vortex-lattice or panel methods and are generally only applied to close-hauled sailing situations where the flow remains attached. Because of the availability of affordable off-the-shelf viscous CFD packages, sail designers are increasingly tempted to use viscous flow solvers for both upwind and downwind sails and masts.

The questions we address in this and ensuing publications is whether commercial viscous CFD codes are indeed suitable for reliable and accurate sail design and performance analysis, what the advantages are of using these codes over the traditional, and much cheaper, panel codes, and which of the turbulence models frequently employed in these codes should be used. In this first work, which was carried out for Team New Zealand's design team, we focussed on upwind sail design. We used the commercial CFD software FLUENT 5.0, and tested the two-equation turbulence models available in this version ($k-\varepsilon$, realizable $k-\varepsilon$, and RNG $k-\varepsilon$). They are summarized in section 2. Near-wall modeling options were also investigated, comparing the performance of wall functions with a near-wall zonal model. The numerical solver used is described in section 3.

Currently there are no 2D or 3D experimental sail flow data available in the public domain that are of sufficient accuracy to be used for code validation. We

Date: September 2002.
Key words and phrases. sail performance analysis, turbulence modeling, RANS.

are in the process of performing suitable wind tunnel tests on various upwind and downwind sail shapes. Preliminary results are reported in [2]. Because of the lack of reliable experimental data, we tested FLUENT's numerical and turbulence models using the challenging backward facing step problem. This problem is well documented and good experimental data are available [18]. The flow past the backward facing step exhibits characteristics similar to the flow past sails at low to moderate angles of attack. We present the results of the validation study in section 4. We note that published backward facing step validation studies do not include accurate results for the RNG and realizable $k-\epsilon$ turbulence models that are reported here. A study is performed in section 5 on two–dimensional sail sections typical of upwind America's Cup sails. We compare the results to the well-known Kennedy-Marsden panel method [9]. In section 6 we discuss a three-dimensional simulation of flow past a genoa and main sail combination, and compare the results to those calculated by Kennedy-Marsden panel method and the Flow97 panel code used at Team New Zealand [5].

We note that all geometries used in this paper are available via correspondence with the authors.

1.1. Predicting a yacht's performance. Predicting which yacht design will give the maximum yacht velocity is difficult. The yacht velocity depends on the size and shape of the hull, sails and appendages, the sea roughness, and the apparent wind speed and direction, amongst others. Velocity Prediction Programs (VPPs) try to capture as many of these effects as possible to accurately predict the maximum velocity made good (the component of the boat's velocity in the direction of the true wind). Key factors in VPPs are performance data on the hull, appendages, rig and sails, usually given in the form of lift and drag characteristics. Traditionally, lift and drag profiles are obtained through prototype testing on the water, or model testing in wind tunnels or towing tanks [6]. Increasingly, Computational Fluid Dynamics (CFD) is used. Because computing flow past the complete yacht is still too arduous a task, most studies focus either on the above water design for given hull and appendages, or the below water design for given rig and sails.

1.2. Typical behavior of flows past sails. Figures 1, 2 and 3 illustrate the typical behavior of flow around two–dimensional sail cross sections for various angles of incidence. In the first figure, the angle of incidence of the apparent wind (true wind-boat velocity) is relatively small. If the sail camber is low and the angle of incidence is close to ideal, i.e. if the flow is incident to the leading edge of the sail, the flow remains attached when it travels over the forward section of the sail. If the angle is slightly greater (or smaller) than ideal, a small recirculation bubble may be formed at the leeward side (or windward side) of the sail with flow reattachment further downstream. In upwind sailing conditions, the sail behaves like an airfoil: The driving force is delivered by the lift force, and the yacht is able to sail "against the wind".

Figure 2 shows a sail at a larger angle of incidence, such as in reaching conditions. The flow is separated near the trailing edge and at the leading edge there is a sizeable separation bubble. In this situation the lift force is almost entirely providing thrust, while the drag acts as a sideways (or heeling) force. Here the design goal is to maximize lift. Fully separated flow (stalled) occurs at high angles of incidence as illustrated in figure 3. In this case drag is a large contributor to the boats thrust.

The Reynolds number of sail flows is high, typically $Re = O(10^6 - 10^7)$, and therefore the flows are turbulent. Accurate simulation of the unsteady separated flows in reaching and downwind conditions is computationally intensive. In this study we investigate upwind sailing situations only. Downwind sail flow simulations are the subject of ongoing research.

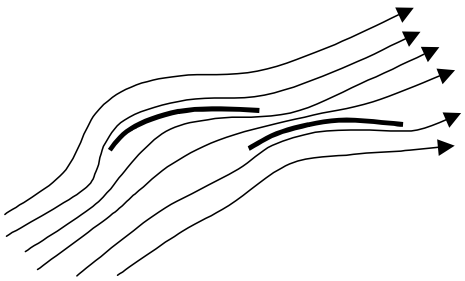

Figure 1. Typical flow in upwind sailing conditions.

As a sail is flexible, its shape cannot be found unless the pressure distribution is known. On the other hand, the pressure cannot be found unless the shape is known. To find the actual flying shape of the sail, the aerodynamics and structural problems must be solved simultaneously. However, in close–hauled situations, in which the sails only have small camber and deform only slightly, fixing the sails is acceptable.

In 3D simulations, we must take into account the logarithmic boundary layer developed over the sea surface. The true wind speed TWS can be modeled as

$$TWS = \frac{u_\tau}{\kappa} \ln \left(\frac{z + z_0}{z_0} \right), \tag{1.1}$$

where z is the distance above the surface, z_0 is a surface roughness length, and $\kappa \approx 0.4$. The friction velocity $u_\tau = \sqrt{\tau_w/\rho_w}$. As a result of this boundary layer profile, the onset flow is twisted: the apparent wind speed and direction and the

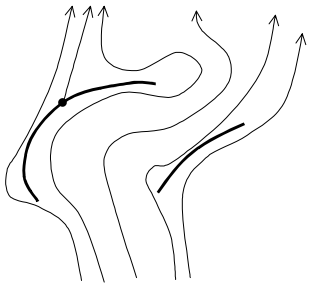

Figure 2. Typical flow in reaching conditions.

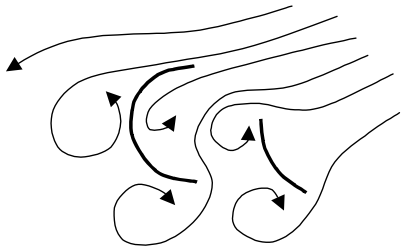

Figure 3. Typical flow in downwind conditions.

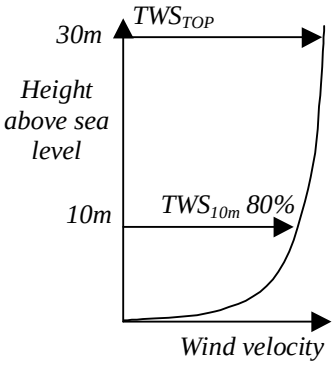

Figure 4. The boundary layer profile of the true wind above the sea surface.

angle of incidence change with z, as shown in the example in figures 4 and 5. Different flow regimes may therefore be observed on the same sail: Near the head of the sail, where there is significant wind twist, the flow is often separated while lower down the flow generally remains attached.

The induced drag, which is drag due to vortex shedding from the head, foot and leech of the sail, is by far the largest type of drag in upwind sail flows. It typically represents over 90% of the drag on the sails and approximately 15% of the total drag on the yacht (including hydrodynamic and aerodynamic forces). Thus, accurate 3D computations seem essential. However, the less computationally intense 2D simulations are still important for selection and validation of turbulence models and numerical solvers. Besides, the initial design of sails is still often done using a series of two–dimensional cross sections. We note that although skin-friction drag constitutes only a small part of the total drag, viscous flow simulations are necessary when flow separation occurs. As discussed below, inviscid flow codes can not predict the location of separation points and may therefore lead to inaccurate lift predictions.

1.3. CFD for sail performance analysis.

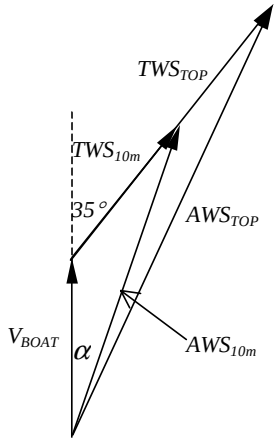

Figure 5. The apparent wind is twisted due to the boat velocity V_{BOAT}. Since the true wind speed at $10m$ (TWS_{10m}) is lower than the true wind speed at the top of the mast (TWS_{TOP}), the apparent wind angle, α, and apparent wind speed, AWS, at $10m$ are smaller than the apparent wind anlge and speed at the top of the mast.

1.3.1. Inviscid codes versus viscous codes in upwind sail design. Currently, the main computational tools used in upwind sail design are inviscid potential flow codes (vortex–lattice or surface panel methods). An overview of these methods is given in [8]. Potential flow codes are relatively cheap to develop, and, if the flow remains attached, the inviscid flow assumption is acceptable. The main advantage of potential flow codes over viscous solvers is that three-dimensional solutions can be obtained in minutes, whereas viscous flow solutions may take many hours to compute. For upwind sails, results obtained with potential flow codes are at least qualitatively correct and can therefore be used to rank potential designs. Therefore, these codes will likely remain the primary tool in industry for upwind sail performance analysis and design for some time. The question we are asking is whether or not viscous CFD codes have a role capturing the finer details of the flow field.

Potential flow codes neglect the viscous boundary layer, and will therefore fail to predict leading edge separation, and possibly also trailing edge separation, for angles larger than the ideal angle. As a result, the performance of the sail will be exaggerated (see also section 5.2.2). We note that because of the twisted wind profile regions of separated flow may exist near the head of a sail, where the angles of attack are higher. Viscous effects can be included by coupling a potential flow model to a viscous boundary layer model [4] which again is generally acceptable if the flow remains largely attached. Otherwise, RANS solvers should be used with appropriate turbulence modeling.

1.3.2. Turbulence modeling. We refer to Wilcox [20] for a thorough discussion of turbulence modeling. Here, we summarize the main points relevant to our discussion.

Both Direct Numerical Simulation (DNS) or Large Eddy Simulation (LES) of the high Reynolds number, wall-bounded turbulent sails flows are computationally too intense for the sail design practice. The most commonly used approach in turbulence modeling is to time–average the Navier–Stokes and continuity equations and solve only for the mean flow variables, thus reducing the grid size and time step constraints. The resulting equations are referred to as the Reynolds Averaged Navier–Stokes (RANS) equations. The averaging process introduces extra terms, commonly known as the Reynolds stresses, in the momentum equations that depend on the turbulent velocity fluctuations and must therefore be modelled. In the popular Boussinesq approximation, the turbulent stresses are modelled as the product of an eddy–viscosity ν_t and a mean strain rate tensor, akin to the molecular gradient–diffusion process. This is intuitive since the net effect of turbulence is to increase the diffusivity of the flow. It leads to turbulence models that are relatively cheap, but have their limitations. For example, the Boussinesq approximation is known to cause difficulties when modeling flow over highly curved surfaces. In reaching or downwind situations, sails generally have high curvature and improved but computationally more intense models, such as second order closure models, may be needed. For upwind sail flows the Boussinesq approximation is deemed appropriate.

2. The flow model

2.1. **The turbulence models.** FLUENT 5.0 gives the user the choice of three $k-\epsilon$ models: The standard model as introduced by Jones and Launder [12]; the Renormalization Group (RNG) model designed by Yakhot and Orszag [22] and the realizable model [17]. For all the models the (steady) equation for the turbulent kinetic energy k can be written in the form,

$$u_i \frac{\partial k}{\partial x_i} = \tau_{ij} \frac{\partial u_i}{\partial x_j} - \epsilon + \frac{\partial}{\partial x_j} \left[(\nu + \nu_T/\sigma_k) \frac{\partial k}{\partial x_j} \right], \tag{2.1}$$

with $\tau_{ij} = 2\nu_T S_{ij}$ ($S_{ij} = \frac{1}{2}(\partial u_i/\partial x_j + \partial u_j/\partial x_i)$, the mean rate-of-strain tensor) and the eddy viscosity, $\nu_T = C_\nu k^2/\epsilon$. Table 5 in appendix A gives the values of σ_k for each of the three $k-\epsilon$ models. The left hand side of the equation gives the advection of turbulent kinetic energy. The first term on the right models the production of k by the mean flow, the second term gives the dissipation of turbulent kinetic energy and the last term represents molecular and eddy diffusion. A full derivation of the equation is given in [20]. The steady ϵ-equation can be written,

$$u_i \frac{\partial \epsilon}{\partial x_i} = C_{\epsilon 1} \frac{\epsilon}{k} \tau_{ij} \frac{\partial u_i}{\partial x_j} - C_{\epsilon 2} \frac{\epsilon^2}{k} + \frac{\partial}{\partial x_j} \left[(\nu + \nu_T/\sigma_\epsilon) \frac{\partial \epsilon}{\partial x_j} \right]. \tag{2.2}$$

The coefficients $C_{\epsilon 1}, C_{\epsilon 2}, \sigma_\epsilon$ and C_ν are shown in table 5 in appendix A. The mathematical surgery involved in closing the ϵ-equation is more drastic than the k equation. As a result many of the shortcomings of the standard $k-\epsilon$ model are due to the inaccuracy of the ϵ equation. The closure coefficients are found through calibration with experimental data for fundamental turbulent shear flows, such as incompressible equilibrium flow past a flat plate. Naturally, the closures are less reliable for complex turbulent flows and care must be taken when interpreting results.

2.1.1. Jones and Launder's k-ϵ model. The standard $k-\epsilon$ model has been the most widely used two–equation model since it was introduced by Jones and Launder [12]. As a result, its strengths and weaknesses are well known. According to Wilcox [20] it is generally inaccurate for flows with adverse pressure gradient (and therefore also for separated flows) which would limit its applicability to sail flows. Also, as is discussed below, the model can not be easily integrated through the viscous sublayer.

2.1.2. RNG k-ϵ model. A more recent version of the $k-\epsilon$ model has been developed by Yakhot and Orszag [22]. Using techniques from renormalization group theory, they developed a new $k-\epsilon$ model which is known as the RNG model. The main difference between the RNG and the standard $k-\epsilon$ models is in the expression for $C_{\epsilon 2}$, which alters the form of the dissipation term. The RNG model decreases dissipation in regions of high mean strain rates. This should make the RNG more suitable for non–equilibrium flows, such as flows with adverse pressure gradients.

2.1.3. Realizable k-ϵ model. The realizable $k-\epsilon$ model was developed by Shih [17]. In the standard $k-\epsilon$ model, the normal Reynolds stress $\overline{u^2}$ becomes negative (non-realizable) when the strain rate is large. Large strain rates can also cause the Schwartz inequality for shear stresses to be violated. To overcome these problems, the realizable $k-\epsilon$ model makes the eddy-viscosity coefficient, C_ν, dependent on the mean flow and turbulence parameters. The notion of variable C_ν has been suggested by many authors and is well substantiated by experimental evidence [16]. For example, C_ν is found to be around 0.09 in the defect layer of an equilibrium boundary layer, but only 0.05 in a strong shear flow We note that in the realizable model, C_ν can be shown to recover this standard value of 0.09 for simple equilibrium flows.

2.2. Near–wall modeling. Approaching the solid boundary, perturbation analysis shows that $k \propto y^2$ and $\epsilon \propto y^0$, thus ϵ is difficult to define. Therefore it is difficult to pose suitable wall boundary conditions for ϵ. When integrating $k-\epsilon$ models through the viscous sublayer solutions are inaccurate unless viscous modifications (damping functions) are applied to the model constants. Incorrect near–wall behavior can severely impact the solution. Two methods are frequently used to correct these inconsistencies. In the wall function approach, the velocity in the first grid point out from the wall is set to its log-law value (see appendix B). Naturally, the numerical solutions are sensitive to the location of this first grid point. Also, the equilibrium wall–functions are not suited to flows with significant pressure gradients. Following Kim et al. [11] a log–law can be derived that is sensitized to pressure–gradient effects. The resulting non–equilibrium wall–functions are available in FLUENT. Alternatively, two-layer models can be used. In FLUENT, the one–equation model of Wolfstein [21] is used in the near–wall region defined by $Re_y \equiv \frac{\sqrt{k}y}{\nu} < 200$. In the rest of the domain the $k-\epsilon$ model of choice is applied. In the Wolfstein model k is computed using equation 2.1, and the eddy viscosity is found using $\nu_t = C_\nu \sqrt{k} l_\nu$, where l_ν is a length scale given by $l_\nu = \kappa C_\nu^{-3/4} y \left(1 - e^{-\frac{Re_y}{70}}\right)$. Specially designed damping functions account for non–equilibrium effects. Potentially, this model gives more accurate results for non–equilibrium flows. However, it has not been used extensively and its accuracy and reliability need to be assessed.

3. The solver

3.1. **The numerical model.** In all tests performed in this paper, the flow equations are discretized with the non-linear third–order Quadratic Upwind Interpolation of Convective Kinematics (QUICK) scheme of Leonard [13]. The discrete equations are solved in an iterative manner to steady-state using the SIMPLE (Semi–Implicit Method for Pressure–Linked Equations) algorithm of Patankar [15]. The solution is declared converged if the average residuals of the continuity, RANS and turbulence equations are below 10^{-4} of their original values.

3.2. **Hardware.** All computations were performed on a single 250MHz R10000 64-bit processor of a SGI Power Challenge XL supercomputer with 3.2Gb of RAM.

4. Benchmarking FLUENT's turbulence models

As was discussed in the introduction, accurate experimental sail flow data are currently not available in the public domain, so that the validity of turbulence models can not be checked directly for sail flows. We therefore choose to benchmark FLUENT's turbulence models using the backward facing step problem which has flow features akin to sail flows (separation bubble, reattachment), and for which reliable experimental data are published in the literature. We remark that to date, published backward facing step validation studies do not include accurate results for the RNG and realizable $k-\epsilon$ turbulence models that are reported here.

4.1. **The backward facing step.** Figure 6 shows a typical velocity profile of flow over the backward facing step used in our experiments. A recirculation region is established downstream of the step. The flow reattaches downstream of the step. The accuracy with which the reattachment length is calculated is an excellent measure of the performance of the turbulence model. Downstream of the reattachment point the flow again reaches equilibrium.

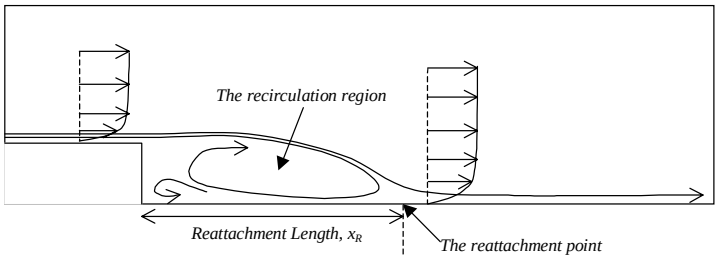

Figure 6. Flow over a backward facing step.

In accordance with the experiments by Westphal, Eaton and Johnson [18], the inlet velocity is taken to be 1.285 m/s. The step height h is set to 1.0 m. The Reynolds number based on step height is 88,000. At the inlet, k and ϵ are calculated using

$$k = \frac{3}{2}(UI)^2, \qquad \epsilon = C_\mu^{3/4}\frac{k^{3/2}}{l}, \tag{4.1}$$

where U is the inlet velocity, I is the turbulent intensity, $C_\nu = 0.09$ and l is the length scale of the turbulent fluctuations. Both I and l are derived assuming fully developed duct flow at the inlet, yielding

$$I = 0.16 \left(Re_e \right)^{-1/8}, \qquad l = 0.07L,$$

with Re_e the Reynolds number of the duct flow which is calculated to be $220,000$, and L the width of the inlet. For this flow, a reattachment length of 8.0 step heights was recorded [18].

We discretized the domain using block–structured grids. An example grid is shown in figure 7. Near the walls the grid cells are long and thin, supplying sufficient resolution in the direction normal to the wall.

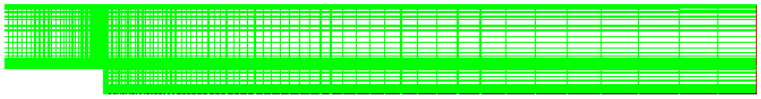

Figure 7. A computational grid for the backward facing step problem (4587 nodes).

A grid convergence analysis was performed using three different grid densities. For the wall–function tests, we used 4587, 18994 and 64002 nodes, essentially halving the grid step sizes each time whilst making sure that the first grid point away from the wall is in the log–layer. The y^+ value at the first grid point was approximately 20 for all of the grids. For the zonal model, where the viscous sublayer must be resolved also, we used two grids with 21859 and 84229 nodes respectively. In these grids the grid densities outside the viscous sublayer correspond to the low and medium density grids in the wall–function tests. A high resolution grid was also tried, but unfortunately converged solutions could not be obtained.

We note that FLUENT conducted a similar backward facing step flow test [10]. However, in our opinion the grids used were too coarse (the number of grid points ranged between 1700 and 6800) to give accurate results.

4.2. Numerical results and analysis. Table 1 shows the computed reattachment lengths for each of the turbulence models using non–equilibrium wall–functions and the zonal model. We note that we also conducted experiments with equilibrium wall–functions but in all cases results were less satisfactory.

Figures 8 through to 11 show the skin friction and the pressure coefficient c_p measured on the lower wall downstream of the step for the low density grids, which gave the best results.

Our findings can be summarized as follows

- The wall–function approach leads to underestimated reattachment lengths and inaccurate c_f and c_p profiles in the recirculation region.
- The zonal model models the recirculation region well and gives improved estimates of the reattachment length.
- The zonal model fails to reach local equilibrium downstream of the reattachment point which will lead to inaccurate lift computations in sail applications.

Non–equilibrium wall functions			
Turbulence model	4,589 nodes	18,994 nodes	64,002 nodes
standard $k-\epsilon$	5.9h	5.9h	5.2h
RNG $k-\epsilon$	6.7h	6.5h	5.9h
realizable $k-\epsilon$	7.0h	6.9h	6.2h
Zonal model			
Turbulence model	21,859 nodes	84,229 nodes	
standard $k-\epsilon$	4.2h	5.2h	
RNG $k-\epsilon$	7.1h	8.6h	
realizable $k-\epsilon$	7.8h	no convergence	

Table 1. Reattachment lengths for the different turbulence models

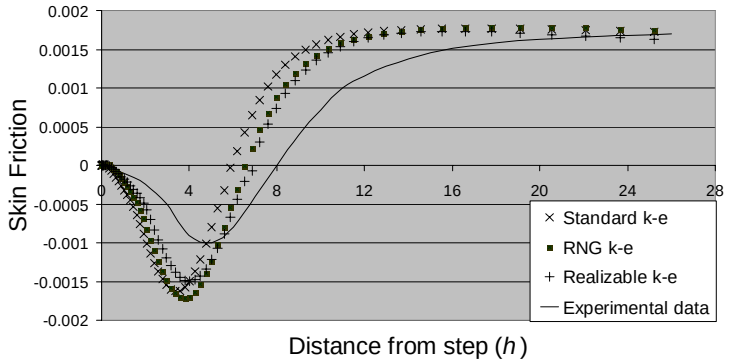

Figure 8. Skin friction on the lower wall, downstream of the step. Computed using wall–functions (4587 nodes).

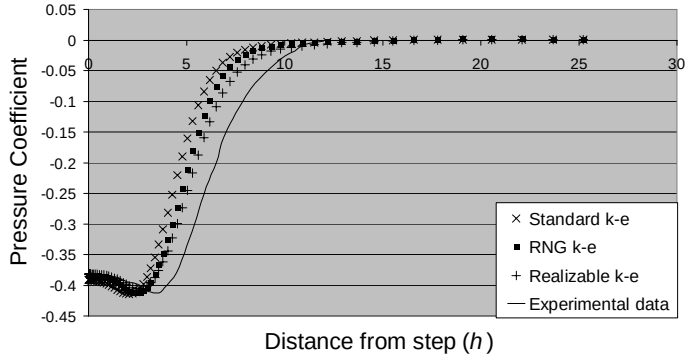

Figure 9. Pressure coefficient on the lower wall, downstream of the step. Computed using wall-functions (4587 nodes).

- For high–resolution grids the c_f and c_p profiles computed by the zonal model show instabilities.

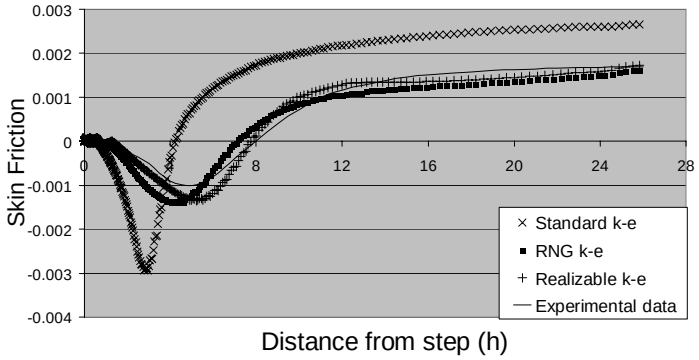

Figure 10. Skin friction on the lower wall, downstream of the step. Computed using the zonal model (21859 nodes).

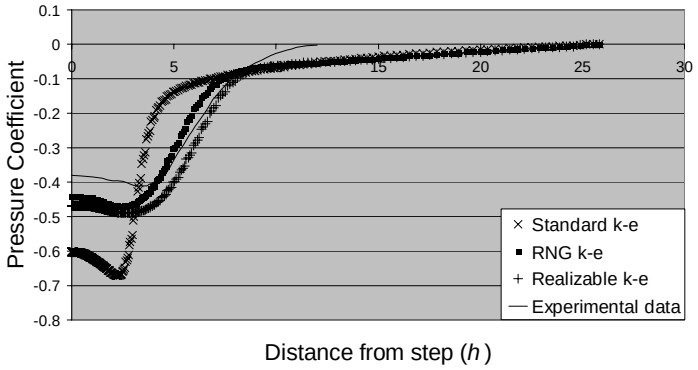

Figure 11. Pressure coefficient on the lower wall, downstream of the step. Computed using the zonal model (21859 nodes).

- Although the y^+ value in the first grid point is kept as close to constant as possible, all results show (some) grid dependency.
- The realizable $k-\epsilon$ model with zonal model fails to converge on the highest resolution grid.
- As expected, the standard $k-\epsilon$ model does not perform well for either the zonal model or the wall–function approach. This is due to over-prediction of the eddy viscosity in regions with adverse pressure gradients which delays separation and accelerates reattachment.
- The RNG and realizable $k-\epsilon$ models provide better results than the standard k-ϵ model, thanks to their modifications for adverse pressure gradient flows. The realizable $k-\epsilon$ outperforms the RNG model.
- Simulation times for the various models are shown in table 2. The RNG model was most expensive. The realizable model took only slightly more time than the standard k-ϵ model.

Non–equilibrium wall–functions on 18,994 nodes grid			
	$k-\epsilon$	RNG	realizable
Iterations	971	1,191	1,081
Time per iteration (s)	5.67	7.11	5.86
Total time (s)	5,505.57	8,468.01	6,334.66
Zonal models on 21,859 nodes grid			
	$k-\epsilon$	RNG	realizable
Iterations	1,081	2,701	1,401
Time per iteration (s)	6.26	6.49	6.32
Total time (s)	6,767.06	17,529.49	8,854.32

Table 2. Performance data

5. Simulation of flows past 2D upwind sails

5.1. The sails and test conditions.

We computed the flow past a two-dimensional horizontal cross section of a genoa and mainsail combination at 18, 22 and 26 degrees angle of incidence. A picture of the genoa and mainsail at 18 degrees is given in figure 14. The ideal angle of incidence of the genoa is approximately 18 degrees. At this angle, the onset flow is incident to the leading edge and the flow remains fully attached. At larger angles a small leading edge separation bubble forms with the flow separating at the leading edge and then reattaching slightly downstream. Thus, for these higher angles, the flow is similar to the flow past the backward facing step. We note that the bubble is short compared to the length of the sail and therefore its influence on the overall drag and lift coefficients is not as great as in the backward facing step case. Separation near the trailing edge may occur too if the angle of incidence is large enough to establish a strong adverse pressure gradient on the top surface of the sail.

The combined length of the genoa and mainsail is 12 m. Figure 12 shows the domain and boundary condition setup. We used a hybrid grid with a structured boundary layer extending 150 mm out from the surfaces of both sails, and an unstructured triangular grid in the remainder of the flow domain as illustrated in figure 13. Long, thin cells are used in the boundary layer where high grid density is only required in the direction normal to the sail boundary. The grid is refined in the tangential direction near the leading and trailing edges of the sails.

At the inflow boundaries the velocity is set at 5 m/s. At the outflow boundaries, a zero gauge pressure is applied. The molecular viscosity is set to $\mu = 1.789\,10^{-5} kgm^{-1}s^{-1}$, leading to a Reynolds number of $Re = 4.1\,10^{6}$. The onset flow does not contain any shear. Therefore, the values for k and ϵ at the inlet are irrelevant; they will quickly decay.

5.2. Numerical results and analysis.

5.2.1. What can we expect?

As noted earlier, flows past sails have similar traits to the flow past the backward facing step. They both have initial separation, recirculation and reattachment. The boundary layer downstream of the reattachment point in the backward facing step case recovers equilibrium. This is not true for sails. Here, an adverse pressure gradient forms that for large enough angles of attack may lead to separation at the trailing edge. For angles close to the ideal angle

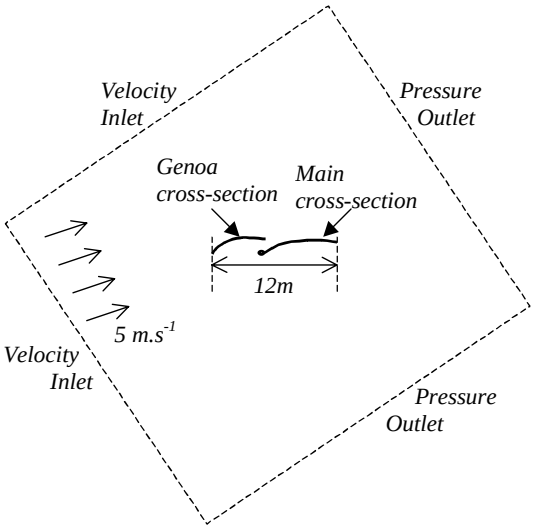

Figure 12. Domain for 2D sail simulations.

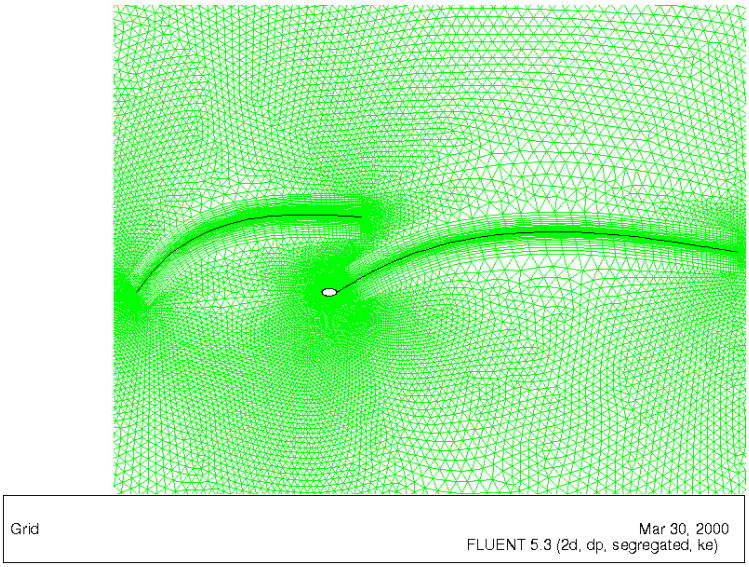

Figure 13. Close-up of computational grid for the 2D sail sections.

of incidence the flow remains attached to the sails, and we expect all models to give reasonable results. For higher angles of incidence, the realizable $k-\epsilon$ model with non–equilibrium wall functions seems the most suitable model of those implemented in FLUENT.

We note that the skin friction results presented in the previous section were of low quality. In sail flows however, skin friction drag is small compared with induced

drag (approximately 10% of induced drag), and constitutes only a small part of the total force on the sail.

5.2.2. Results. For the solution at ideal angle of attack (18°) all models return the lift coefficient C_L = 1.67 and drag coefficient C_D = 0.11. The force coefficients were accurate over all turbulence models and all grid densities indicating model consistency and grid convergence. In this test case the mean strain rates are much lower than for the backward facing step and consequently the turbulence models are in agreement. Figure 14 shows the corresponding streamlines.

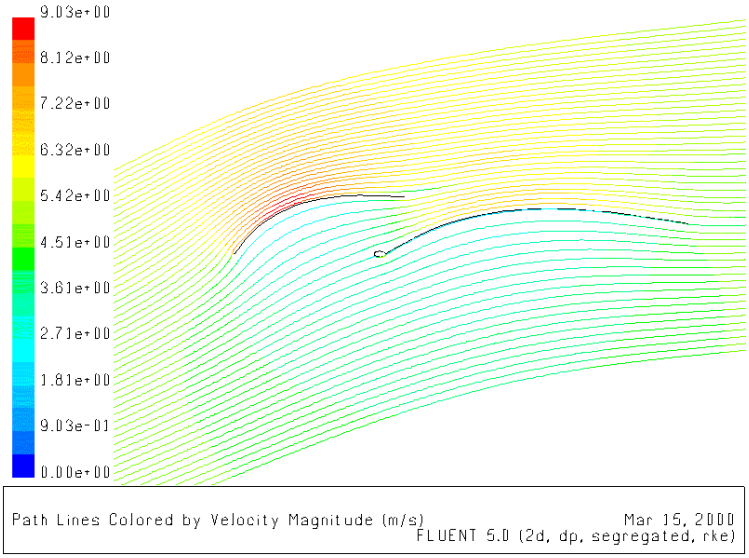

Figure 14. Streamlines for two-dimensional sail sections at ideal angle of incidence (18 degrees).

Figure 15 shows the computed flow at an angle of incidence of 22 degrees. As expected, the flow separates at the leading edge of the genoa, and forms a separation bubble on the forward section of the leeward surface of the sail. At 26 degrees, the flow also separates near the trailing edge as shown in figure 16.

Table 3 gives computed lift and drag coefficients for the realizable $k-\epsilon$ model at 22 and 26 degrees using the non–equilibrium wall-function as well as the zonal model approach. As in the backward facing step experiments, the zonal model computes a longer recirculation area leading to higher drag and lower lift than expected. Also, as before, the realizable and RNG $k-\epsilon$ models predict flows with longer separation bubbles than the standard $k-\epsilon$ model.

5.2.3. Comparison to panel method. Comparisons were made between the FLUENT solutions and the well-tested Kennedy-Marsden panel method with Lan-Stark panel distribution [9]. The force coefficients are presented in table 4. The comparison shows that near ideal angle of attack the inviscid panel method performs reasonably well. At 18 degrees lift is overestimated by 16.7% and the method predicts zero drag (approximately) as it should do according to potential flow theory. As the angle of attack increases the lift coefficient is increasingly overpredicted by the

Angle of incidence	near wall model	c_d	c_l
22	non–equilibrium wall function	0.1663	1.9541
22	zonal model	0.1713	1.9375
26	non–equilibrium wall function	0.2433	2.1732
26	zonal model	0.2965	2.0779

Table 3. Lift and drag coefficients for realizable $k-\epsilon$ model with non–equilibrium wall functions and zonal model.

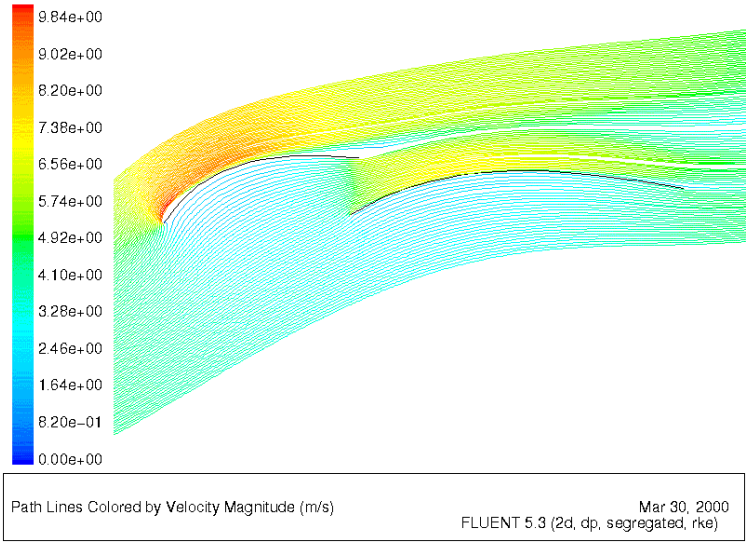

Figure 15. Streamlines for angle of incidence of 22 degrees (realizable $k-\epsilon$ with non-equilibrium wall functions).

Angle of incidence	FLUENT		Panel Method	
	c_l	c_d	c_l	c_d
18	1.67	0.11	1.95	0.06
22	1.94	0.17	2.40	0.13
26	2.17	0.24	2.84	0.26

Table 4. Comparison of lift and drag coefficients from FLUENT solutions and panel method solutions.

panel method. In the viscous CFD solutions the boundary layer thickens as the angle increases which results in a loss in circulation and thus also a loss in lift. This viscous effect is not accounted for in the panel method. The ideal angle of attack predicted by the panel method is too low (15 degrees instead of 18) which is a direct result of the exaggerated lift and hence an overprediction of the upwash upstream of the sail. Consequently the leading edge of the sail sees a larger angle of attack than would be expected in a viscous flow.

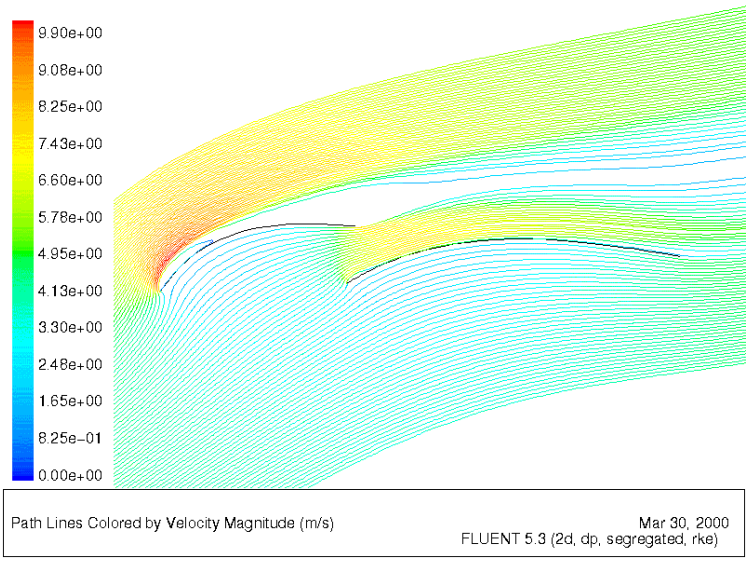

Figure 16. Streamlines for angle of incidence of 26 degrees (realizable $k-\epsilon$ with non-equilibrium wall functions).

In the panel method the lift coefficient increases linearly with angle of attack, and there is no evidence of stall. It is also interesting to note that at high angles of attack the panel method predicts nonzero drag coefficients which illustrates the difficulties the method has at these angles.

We conclude that the realizable $k-\epsilon$ model with non–equilibrium wall functions is acceptable and accurate at low angles of attack and thus for close–hauled upwind sailing situations. At low angles of attack the realizable $k-\epsilon$ model provides solutions consistent with the other $k-\epsilon$ turbulence models implemented in FLUENT. At higher angles of attack the model can be trusted to predict leading edge separation, boundary layer recovery and trailing edge separation more reliably than the other $k-\epsilon$ FLUENT models. This is evident from its superior performance for the flow past the backward facing step.

6. Three–dimensional simulations

6.1. **The sails and test conditions.** The sail shapes investigated are typical IACC genoas and main sails from the Team New Zealand sail design program. The physical domain is shown in figure 17. The sails are rotated 25 degrees to leeward representing the heeling action of the boat. Only the sails themselves are included in the geometry, not the hull, rigging or mast. We note that induced drag will be somewhat overestimated in our calculations without the deck under the sails to limit pressure leakage around the foot.

The bottom of the domain represents the (flat) sea surface. On this surface we impose a no-slip boundary condition. The back and leeward boundaries are modelled as pressure outlet boundaries to which zero gauge pressure is applied.

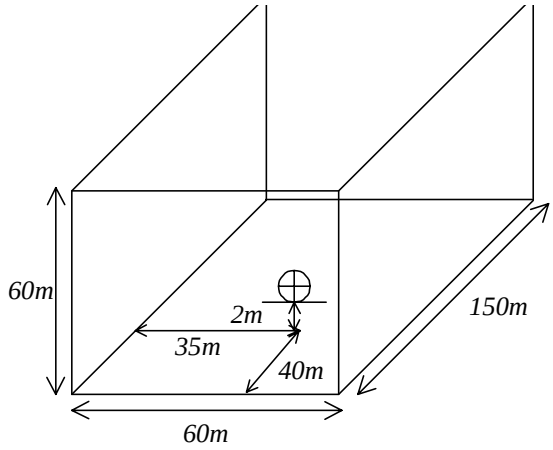

Figure 17. 3D domain used in the simulations. The cross indicates the position of the sails.

As discussed in the introduction, the onset flow satisfies the logarithmic boundary layer profile given by equation 1.1. The values of u_τ and z_0 are chosen such that the wind speed at $10m$ above sea level is 80% of the free stream value and 100% at $30m$ above sea level. These values correspond to on the water measurements. The free stream wind velocity is set at $6.5m/s$ which is typical of Auckland conditions. The true wind angle is taken to be 35 degrees which is typical of IACC boats when sailing upwind. The boat is assumed to be travelling at a constant speed of $4.5m/s$. This leads to an angle of incidence of 18.8 degrees at 10 m above sea level and 20.8 degrees at the head of the sails.

Using a length scale of 21 m (the combined length of the mainsail foot and genoa foot) the Reynolds number of the flow is computed to be $Re = 9.35\ 10^6$. Inflow boundary conditions for k and ϵ are calculated to be 0.03375 and 0.36386 respectively, based on a freestream intensity of 3%, which is a typical value for the University of Auckland twisted flow wind tunnel.

Near the head of the genoa, the main sail and genoa are in very close proximity. The automatic grid generator in FLUENT failed to create a structured boundary layer grid in this area, and a triangular face mesh had to be created instead. The domain is meshed with tetrahedral cells. Due to the resulting memory limitations the grid spacing had to be restricted to 75 mm on the sail surface, with corresponding y^+ values for the grid points closest to the surface between 300 and 600. The grid density was therefore insufficient. The grid contained 429,589 grid points and 2,098,263 grid cells.

6.2. Numerical results and analysis. The flow was computed using the realizable $k-\epsilon$ model with non–equilibrium wall functions. Figure 18a shows pathlines released from the leeward surfaces of the genoa and main sail. Figure 18b depicts pathlines at $25m$ above sea level, viewed from the front of the main sail. The swirling flow leaving the foot and head of the sails are tip vortices that cause induced drag. Towards the top of the main sail the flow can be seen to separate caused by the larger angle of incidence, whereas closer to the foot of the sail the

flow is attached. This is also clear from figures 19a and b. We note that the head of the genoa is just below $25m$ above sea level. The tip vortices of the genoa create an upwash on the flow over the main sail which leads to a further increase in angle of incidence.

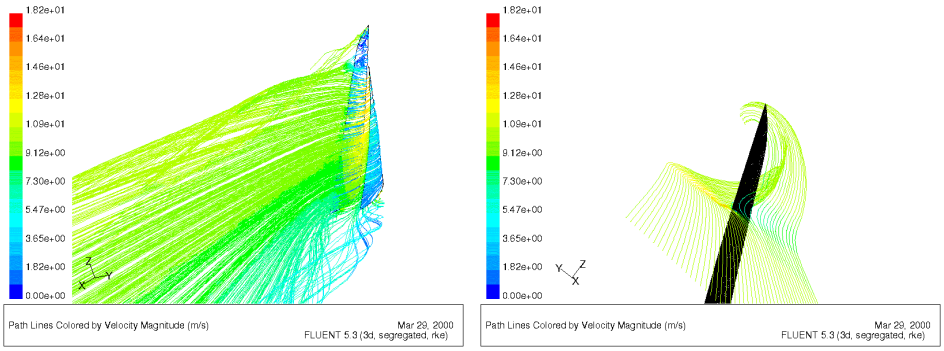

a. b.

Figure 18. a. Streamlines released from the leeward sail surfaces; b. Streamlines at $z = 25m$, viewed from upstream of the mainsail with the genoa hidden.

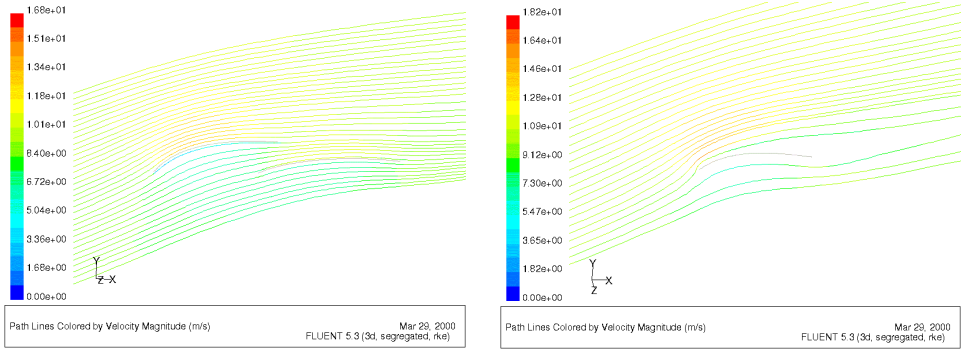

a. b.

Figure 19. Streamlines in horizontal cutting plane: a. at $z = 10m$; b. at $z = 25m$.

The computed lift and drag coefficients are 1.15 and 0.14, respectively. The coefficients computed by Team New Zealand using their well-tested and calibrated Flow97 panel code are 1.25 and 0.14, respectively [5]. Again, the panel method overpredicts the lift, as expected. Because the drag coefficients of the viscous solver includes skin friction drag, the induced drag calculated by Flow97 is actually larger than the induced drag computed by FLUENT. This follows from the higher predicted lift and an increased loading of the head of the sail in the Flow97 case.

The solutions shown are qualitatively correct. However, results from the previous sections showed us that we can not entirely trust the lift and drag coefficients computed in this simulation because of insufficient grid resolution and the inaccuracy of the standard $k-\epsilon$ models for separated flows.

The solution took approximately 72 hours to converge.

7. Conclusions and recommendations

From our numerical experiments, we conclude that

- RANS solvers are necessary to accurately predict lift and drag coefficients for separated sail flows. The RANS results compare favorably to results calculated by traditional panel methods.
- The two–equation $k-\epsilon$ turbulence models tested have the potential to provide accurate results for flow around close hauled upwind sails, provided the flow remains predominantly attached (so angle of incidence is close to ideal), and the grid density is sufficient in the boundary layer with y^+ values within the required range.
- The realizable $k-\epsilon$ model with non–equilibrium wall functions is the most appropriate of the models tested for apparent wind angles that are slightly larger than ideal.
- The two-equation $k-\epsilon$ models tested are not expected to produce reliable results for sail flows at larger angles of attack.
- The non-equilibrium wall functions tested are preferred over the zonal models.

Although the $k-\epsilon$ models produce adequate results for attached sail flows, simpler models such as the frequently used Spalart–Allmaras one–equation model [19] or even the Baldwin–Lomax zero–equation model [1], are expected to perform just as well for these (simple) flows at lower costs. For separated sail flows, we advise the use of models that can be accurately integrated through the viscous sublayer. A literature review indicates that suitable candidates are the 1998 Wilcox $k-\omega$ model [20], and Menters BSL and SST models [14]. As reported in these references, these models are suitable for flows with (strong) adverse pressure gradients and flow separation. These two models are commonly used for analysis of high-lift airfoils where the design goal is to maximize lift, while paying little attention to drag. For these foils the flow is frequently separated and it is frequently reported that in such circumstances the SST model is the most appropriate. Both the SST model and the Wilcox $k-\omega$ model will be included in the next version of FLUENT and are also now available in other commercial packages, such as CFX. A thorough turbulence modeling literature survey and analysis is presented in [3] that can be obtained from the authors.

For downwind flows these models may still be inaccurate and a higher-order model may be necessary. For highly curved downwind flows there may be enough streamline curvature to cause the Reynolds stress tensor to be anisotropic, thus invalidating the Boussinesq approximation. In such a situation either a non-linear eddy viscosity model or a second-order closure model may be necessary. Currently work is being carried out comparing CFD solutions (using CFX-5.5) for highly cambered downwind sail sections (up to 25% camber) with accurate wind tunnel tests that are currently being carried out. For these downwind flows the boundary

layer is attached for just 50% of the sails length and the flow is unsteady. At small angles of attack periodic vortex shedding is evident, whereas at high angles near complete stall (where the leading edge bubble fails to reattach) the wake is chaotic. Preliminary results are reported in [2].

We remark that flow visualization provided valuable insight into the structure of sail flows that proved helpful in the sail design process.

8. Acknowledgements

This project was sponsored by the Technology New Zealand under the Graduates in Industry Fellowship TEA801. We would like to thank Nick Holroyd, Tom Schnackenburg and Burns Fallow of Team New Zealand for their guidance and for providing the geometry files for the sail shapes.

Appendix A. Closure coefficients

	$C_{\epsilon 1}$	$C_{\epsilon 2}$	C_μ	σ_k	σ_ϵ
Standard	1.44	1.92	0.09	1.0	1.3
RNG	1.42	$\tilde{C_{\epsilon 2}} + \frac{C_\mu \lambda^3 (1-\lambda/\lambda_O)}{1+\beta\lambda^3}$ $\tilde{C_{\epsilon 2}} = 1.68, : \lambda = \frac{k}{\epsilon}\sqrt{2S_{ij}S_{ji}},$ $: \beta = 0.012, \lambda_O = 4.38$	0.085	0.72	0.72
Realizable	$\max\left(0.43, \frac{\lambda}{\lambda+5}\right)$ $\lambda = \frac{k}{\epsilon}\sqrt{2S_{ij}S_{ji}}$	1.9	$\left(A_O + A_s \frac{k\sqrt{S_{ij}S_{ij}}}{\epsilon}\right)^{-1}$ $A_O = 4.04,$ $: A_s = \sqrt{6}\cos\left(\frac{1}{3}\arccos\sqrt{6}W\right),$ $W = \frac{S_{ij}S_{jk}S_{ki}}{\sqrt{S_{ij}S_{ij}}}$	1.0	1.2

Table 5. Coefficients for the k and ϵ equations

Appendix B. The log-law of the wall

The velocity follows a logarithmic profile in the log–layer (known as the log-law) given by

$$u^+ \approx \frac{1}{\kappa} \ln y^+ + B, \tag{B.1}$$

where the Karman constant $C \approx 0.41$, and $C \approx 5$ for smooth surfaces. Here u^+ and y^+ are the scaled velocity and distance to the wall defined by

$$u^+ \equiv \frac{u}{u_\tau}, \qquad y^+ \equiv \frac{u_\tau y}{\nu}. \tag{B.2}$$

The values of k and ϵ in the log-layer are determined using $k = u_\tau^2/\sqrt{\beta}$ and $\epsilon = (\beta)^{3/4}k^{3/2}/\kappa y$.

References

[1] B. S. Baldwin and H. Lomax. Thin layer approximation and algebraic model for separated turbulent flows. AIAA Paper 78–257, 1978.

[2] Jackson P. Collie, S. and M. Gerritsen. Design of two-dimensional downwind sail sections using computational fluid dynamics. In High Performance Yacht Design Conference, 2002.

[3] S. Collie and M. Gerritsen. An investigation into turbulence models for sail flows. Technical report, Department of Engineering Science, University of Auckland, 2001.

[4] M. Drela. Xfoil 6.8 user primer. Technical report, M.I.T. Aero and Astro, Boston, 1996.

[5] B. Fallow. Private communication.

[6] R.G.J. Flay. A twisted flow wind tunnel for testing yacht sails. Journal of Wind Engineering and Industrial Aerodynamics, 63, 1996.

[7] R. G. J Flay (editor). Sail aerodynamics. Special issue of the Journal of Wind Engineering and Industrial Aerodynamics, 63, 1996.

[8] J. Katz and A. Plotkin. Low-Speed Aerodynamics. From Wing Theory to Panel Methods. McGrawHill Inc, 1991.

[9] J. L. Kennedy and D. J. Marsden. Potential flow velocity distribution on multi-component airfoil sections. Canadian Aeronautics and Space Journal, 22(5), 1976.

[10] Mathur S.R. Murthy J.Y. Kim, S-E and D. Choudhury. A reynolds-averaged navier-stokes solver using an unstructured mesh based finite volume scheme. Technical Report TN117, FLUENT Inc., 1997.

[11] S.-E. Kim and D. Choudhury. A near–wall treatment using wall functions sensitized to pressure gradient. AMSE FED Separated and Complex Flows, 217, 1995.

[12] B.E. Launder and D.B. Spalding. The numerical computation of turbulent flows. Computer Methods in Applied Mechanics and Engineering, 3:269–289, 1974.

[13] B.P. Leonard. A stable and accurate convective modelling procedure based on quadratic upstream interpolation. Computational Methods in Applied Mechanics and Engineering, 19:59–98, 1979.

[14] F. R. Menter. Zonal two–equation $k-\omega$ turbulence models for aerodynamics flows. AIAA Paper 93–2906, 1993.

[15] S.V. Patankar and D.B. Spalding. A calculation procedure for heat, mass and momentum transfer in three-dimensional parabolic flows. International Journal of Heat and Mass Transfer, 15, 1972.

[16] O. Reynolds. An experimental investigation of the circumstances whcih determine whether the motion of water shall be direct or sinuous, and of the law of resistance in parallel channels. Royal Society Phil. Trans., 1883.

[17] Lion W.W. Shabbir A. Shih, T.H. and J. Zhu. A new k-epsilon eddy-viscosity model for high reynolds number turbulent flows - model development and validation. Computers and Fluids, 24(3):227–238, 1995.

[18] R. M. C. So and Y.G. Lai. Low–reynolds–number modelling of flows over a backward facing step. Journal of Applied Mathematics and Physics, 39:13–27, 1988.

[19] P. R. Spalart and S. R. Allmaras. A one–equation turbulence model for aerodynamics flows. La Recherche Aerospatiale, (1):5–21, 1994.

[20] D.C. Wilcox. Turbulence Modeling for CFD, 2nd Edition. Griffin Printing, California, 1998.

[21] M. Wolfstein. The velocity and temperature distribution of one–dimensional flow with turbulence augmentation and pressure gradient. International Journal of Heat and Mass Transfer, 12:301–318, 1969.

[22] V. Yakhot and S. Orszag. Renormalization group analysis of turbulence: I. basic theory. Journal of Scientific Computing, 1(1):1–51, 1986.

Yacht Research Unit, Auckland University, New Zealand
E-mail address: steve.collie@xtra.co.nz

Stanford Yacht Research, Stanford University
E-mail address: margot.gerritsen@stanford.edu
URL: http://syr.stanford.edu